Phase Transitions in Inorganic Halide Perovskites from Machine-Learned Potentials

THE JOURNAL OF PHYSICAL CHEMISTRY C
A JOURNAL OF THE AMERICAN CHEMICAL SOCIETY

pubs.acs.org/JPCC

Article

Phase Transitions in Inorganic Halide Perovskites from Machine-Learned Potentials

Erik Fransson,* Julia Wiktor, and Paul Erhart*

Cite This: *J. Phys. Chem. C* 2023, 127, 13773−13781

Read Online

ACCESS | Metrics & More | Article Recommendations | Supporting Information

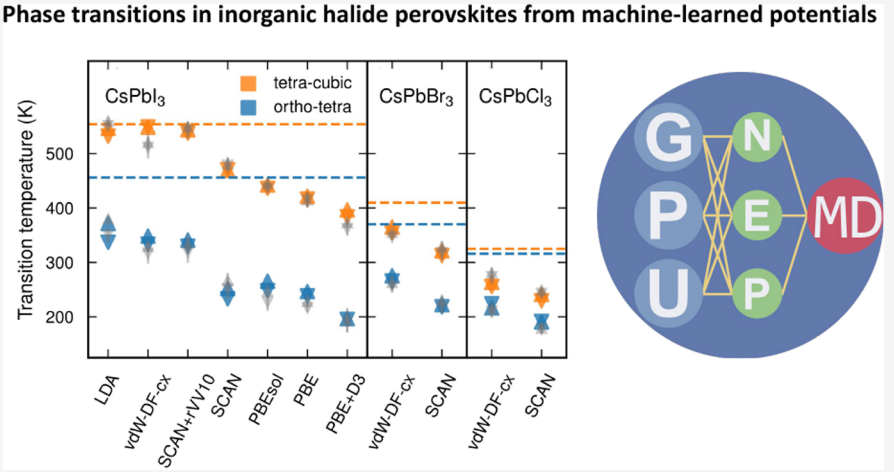

ABSTRACT: The atomic scale dynamics of halide perovskites have a direct impact not only on their thermal stability but also on their optoelectronic properties. Progress in machine-learned potentials has only recently enabled modeling the finite temperature behavior of these materials using fully atomistic methods with near first-principles accuracy. Here, we systematically analyze the impact of heating and cooling rate, simulation size, model uncertainty, and the role of the underlying exchange-correlation functional on the phase behavior of $CsPbX_3$ with X = Cl, Br, and I, including both the perovskite and the δ-phases. We show that rates below approximately 60 K/ns and system sizes of at least a few tens of thousands of atoms should be used to achieve convergence with regard to these parameters. By controlling these factors and constructing models that are specific for different exchange-correlation functionals, we then assess the behavior of seven widely used semilocal functionals (LDA, vdW-DF-cx, SCAN, SCAN+rVV10, PBEsol, PBE, and PBE+D3). The models based on LDA, vdW-DF-cx, and SCAN+rVV10 agree well with experimental data for the tetragonal-to-cubic-perovskite transition temperature in $CsPbI_3$ and also achieve reasonable agreement for the perovskite-to-delta phase transition temperature. They systematically underestimate, however, the orthorhombic-to-tetragonal transition temperature. All other models, including those for $CsPbBr_3$ and $CsPbCl_3$, predict transition temperatures below the experimentally observed values for all transitions considered here. Among the considered functionals, vdW-DF-cx and SCAN+rVV10 yield the closest agreement with experiment, followed by LDA, SCAN, PBEsol, PBE, and PBE+D3. Our work provides guidelines for the systematic analysis of dynamics and phase transitions in inorganic halide perovskites and similar systems. It also serves as a benchmark for the further development of machine-learned potentials as well as exchange-correlation functionals.

INTRODUCTION

Halide perovskites are among the most intensively studied materials of the past decade due to their attractive properties for applications in, for example, solar energy harvesting and lighting.[1−4] Similar to their oxide counterparts, many of these materials exhibit several different phases that are connected through soft modes and continuous or weak first-order phase transitions.[5,6] This complex dynamic behavior turns out to be intimately connected to their remarkable optoelectronic properties.

In this context, electronic structure calculations play a crucial role, as they can provide detailed insight into the atomic scale dynamics and microscopic coupling mechanisms. Static calculations can, however, only provide limited information

Received: March 7, 2023
Revised: June 14, 2023
Published: July 5, 2023

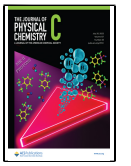

due the strong anharmonicity associated with the soft modes.[7−10] This has motivated a number of dynamic studies based on *ab initio* molecular dynamics (MD) simulations[11−18] and, more recently, machine-learned potentials (MLPs).[19−28] From such simulations one can then obtain, for example, transition temperatures[19] or structural information at finite temperatures.[11,18,29]

The accuracy of such simulations is, however, limited by several factors, most notably (1) sampling time, (2) system size, (3) the quality of the exchange-correlation (XC) functional, and, in the case of MLPs, (4) the model uncertainty. Sampling time and system size are, in particular, a problem for *ab initio* MD simulations, which are typically limited to time scales of a few tens of picoseconds and system sizes on the order of 1000 atoms. Previous MLP based studies were able to extend these ranges to total run times of a few nanoseconds using about a thousand atoms.[19,20,26]

Here, we carry out a systematic analysis of the four factors described above. We consider $CsPbX_3$ with X = Cl, Br, and I and the local-density approximation (LDA), van der Waals density functional with consistent exchange (vdW-DF-cx),[30,31] strongly constrained and appropriately normed (SCAN),[32] SCAN+rVV10,[33] PBEsol,[34] PBE,[35] and PBE+D3[35,36] XC functionals. The selection of these functionals is motivated by the fact that they were constructed using physical constraints in order to minimize empiricism. As a result, they have commonalities but also exhibit some differences in their design logic, making it interesting to contrast their performance. The potential energy surface PES is mapped using third-generation neuroevolution potential (NEPs) models and sampled using the GPUMD package. The latter provides an efficient neuroevolution potential (NEP) implementation that enables us to routinely sample systems comprising on the order of 60000 atoms for 100 or more nanoseconds.

We show that well converged results can be achieved using systems containing several ten thousand atoms and heating/cooling rates on the order of 60 K/ns or lower. Using bootstrapping and ensembles of models, we are able to readily generate accurate NEP models with an uncertainty that is comparable or lower than the training errors.

By controlling rate and size effects as well as model errors, we are able to isolate the impact of the underlying XC functionals and thus to quantitatively assess the quality of different XC functionals for the description of phase transitions and finite temperature properties of halide perovskites. We find the vdW-DF-cx functional to perform the best among the XC functionals considered here when comparing transition temperatures and lattice constants to the experimental data.

In the following section, we analyze in order rate and size effects (see the "Rate and Size Effects" section), mode uncertainty (see the "Model Uncertainty" section), the impact of the XC functional (see the "Impact of XC Functional and Extension to Other Halides" section), and finally the transition temperature between the δ and perovskite phases (see the "Transition to δ-Phase" section). We then summarize and discuss the outcome of this analysis (see the "Discussion" section).

METHODS

Machine-Learned Potentials. *Neuroevolution Potentials.* Here, we use the third generation of the NEP scheme (NEP3)[37] to build MLPs for $CsPbX_3$ with X = Cl, Br, and I. The NEP format employs a simple multilayer perceptron neural network architecture with a single hidden layer.[38] In NEP3 the radial part of the atomic environment descriptor is constructed from linear combinations of Chebyshev basis functions, while the three-body angular part is similarly built from Legendre polynomials. Four- and five-body terms of the atomic cluster expansion form[39] can be included as well, but here we limit ourselves to two and three-body terms.

For the present purpose it is crucial that the NEP scheme is not only accurate but has been implemented on graphical processing units (GPUs) in the GPUMD package.[37] For the models described in the following, this allows us to achieve a speed of 2×10^7 atom step/s on an NVidia A100 card, i.e., we can simulate a system of 60000 atoms for about 150 ns per day using a time step of 5 fs.

Computational Parameters. In this study we used the same hyperparameters for all models, which were chosen based on experience and pretrials.[37] The cutoffs for two- and three-body interactions are 8 and 4 Å, respectively. There are 8 radial and 6 angular descriptor components and 8 basis functions for building both the radial and angular descriptor functions, and the angular components are expanded up to fourth order. The hidden layer contains 40 neurons.

The weights for energies, forces, and virials in the loss function were set to 1, 1, and 0.1 in GPUMD units, respectively, while the weights for the l_1 and l_2 regularization terms were dynamically adjusted during the optimization. The neuroevolution strategy[40] employed for optimizing the parameters used a population size of 50 and was run for 200000 generations.

Model Construction. To construct NEP models, we employed a boot-strapping strategy. First we identified potentially relevant phases. This included the cubic perovskite structure ($Pm\bar{3}m$, Glazer notation $a^0a^0a^0$), two tetragonal structures ($I4/mcm \rightarrow a^0a^0c^-$, $P4/mbm \rightarrow a^0a^0c^+$), representing out-of-phase and in-phase tilts relative to the c-axis, respectively, one orthorhombic structure ($Pnma \rightarrow a^-a^-c^+$) as well as the so-called delta-phase ($Pnma$), which is experimentally known to be the most stable structure at least for $CsPbI_3$ and $CsPbBr_3$.

We then calculated energy-volume curves for these five prototype structures using density functional theory (DFT) calculations (see the "Reference Calculations" section) allowing both the ionic coordinates and the cell shape to relax under the constraint of constant volume until the maximum force on any atom fell below 30 meV/Å.

Subsequently we generated supercells for each prototype with random atomic displacements using the Monte Carlo rattle procedure from the HIPHIVE package[41] with a standard deviation of 0.04 Å. The supercell size was chosen to be between 120 and 160 atoms, and the volume was varied between 85% and 110% of the respective equilibrium volume with five structures per volume and prototype.

Using these data we generated a first iteration of NEP models using the GPUMD package for the optimization[37] and the CALORINE package for data preparation and analysis.[42] One model was generated using the full data set ("full model") and five additional models ("model ensemble") were generated by using five different 90−10 splits of the available data. Using the full model, we generated new structures for each prototype by running short MD simulations at pressures between −1 and 10 GPa using a temperature ramp from 20 to 620 K over 3 ns. From each trajectory, we selected 12 configurations. For each of these configurations, we then computed the standard

https://doi.org/10.1021/acs.jpcc.3c01542
J. Phys. Chem. C 2023, 127, 13773−13781

deviation of the energy and forces using the model ensemble. The standard deviation over the ensemble predictions provided a measure for the uncertainty of the current model generation for the respective conditions (temperature, pressure, structure). We then computed energy and forces for the new structures using DFT calculations, added these to the training set, and repeated the procedure. Typically after four generations we found that the uncertainty in the energy and forces were comparable, which are smaller than the respective training error, indicating convergence of the model construction.

We note that in principle, one could have adapted an active learning strategy based on the model ensemble and only included configurations with high uncertainty as additional reference structures. Here, we decided to include rather more data in the training set, but we expect that the number of structures can be reduced considerably without a notable decrease in model performance.

The final models yield RMSE scores for training and validation sets of about 1, 50, and 12 meV/atom or better for energies, forces, and virials, respectively (Tables 1 and S1).

Table 1. RMSE Scores for the Final NEP Models Obtained by Training against the Full Data Set[a]

	energy (meV/atom)	force (meV/Å)	virial (meV/atom)
$CsPbBr_3$			
vdW-DF-cx	0.6	46.0	8.5
SCAN	0.7	49.3	12.2
$CsPbCl_3$			
vdW-DF-cx	0.7	48.1	9.7
SCAN	0.7	49.5	12.7
$CsPbI_3$			
LDA	0.9	47.6	10.8
vdW-DF-cx	1.2	49.1	11.6
SCAN	1.6	52.5	13.9
SCAN +rVV10	1.5	52.3	13.3
PBEsol	1.2	51.3	12.0
PBE	0.7	43.7	9.6
PBE+D3	0.8	44.4	9.4

[a]Additional performance measures, including RMSE and Pearson correlation coefficients for model ensembles, can be found in Table S1.

Importantly the models closely reproduce the energy differences and energy-volume curves of all the structures of interest in the present study (Figures S1 and S2; Tables S2−S7). The final models were subsequently used in large scale MD simulations to predict, for example, transition temperatures and lattice parameters (see the "MD Simulations" section).

MD Simulations. All MD simulations were carried out using the GPUMD code. Temperature and pressure were controlled using stochastic velocity[43] and cell rescaling[44] and the time step was 5 ps, where all simulations were run at zero pressure.

For studying the convergence with size (see the "Size effects" section), we considered system sizes between 1280 and 61440 atoms, equivalent to 4 × 4 × 4 to 16 × 16 × 12 primitive orthorhombic perovskite (20-atom) unit cells. To analyze the impact of heating and cooling rates (see the "Rate Effects" section) the temperature was linearly varied between 20 and 520 to 620 K (depending on material) over 1−100 ns. The production runs used to quantify model uncertainty (see the "Model Construction" section) and the impact of the XC functional (see the "Impact of XC Functional and Extension to Other Halides" section) were carried out using supercells comprising 16 × 16 × 12 primitive orthorhombic unit cells (61440 atoms). The total simulation time was set to 100 ns, and the temperature was varied over a range of 400 to 600 K corresponding to a heating/cooling rate of 4−6 K/ns.

Free Energy Calculations. For $CsPbI_3$ and possibly $CsPbBr_3$ the perovskite phases are metastable only at lower temperatures. Provided sufficient kinetic activation, below a certain temperature, the perovskite structure transforms into the so-called δ-phase via a first order transition. To determine the transition temperature from the NEP models we calculated the free energies of the δ and cubic perovskite phases through thermodynamic integration using the classical method by Frenkel and Ladd,[45−47] as implemented in ASE.[48] In these calculations, we used an Einstein solid as a reference system, for which the free energy can be computed analytically, and used supercells containing about 1500 atoms for each phase. For each temperature the integration was carried out over 50 ps, and the results were averaged over ten independent runs.

Reference Calculations. DFT calculations were performed using the projector augmented-wave method[49] as implemented in the Vienna ab initio simulation package.[50,51] The exchange-correlation contribution was represented using the LDA, the vdW-DF-cx method,[30,31] the SCAN functional,[32] the SCAN+rVV10 functional,[33] the PBEsol functional,[34] the PBE functional,[35] and the PBE functional with dispersion corrections (PBE+D3).[35,36] The Brillouin zone was sampled with a Γ-centered grid with a k-point density of 0.18 /Å and Gaussian smearing with a width of 0.1 eV. For the calculation of the forces, a finer support grid was employed to improve their numerical accuracy.

RESULTS

Rate and Size Effects. The different perovskite phases are structurally closely related and connected through phase transitions with mixed continuous-first-order character.[52−55] For the $CsPbX_3$ (with X = Cl, Br, or I) materials considered in this study, the perovskite lattice transforms with increasing temperature from an orthorhombic phase ($Pnma$) via a tetragonal phase ($P4/mbm$) to a cubic phase ($Pm\bar{3}m$). Since these transitions do not involve a switch in the sign of the Glazer angles between the orthorhombic ($a^-a^-c^+$) and tetragonal phases ($a^0a^0c^+$), unlike, e.g., $MAPbI_3$,[19] it is possible to observe these transitions in MD simulations. Due to the remaining first-order character and the extreme heating/cooling rates that can be realized in MD simulations, one can, however, nonetheless anticipate some degree of hysteresis.

A further aggravating factor is the finite system size. For small supercells, the fluctuations are naturally larger, which renders it more challenging to achieve converged results. In this section, we discriminate the effects of heating/cooling rate and system size by considering in detail MD simulations for $CsPbI_3$ using the full model based on the vdW-DF-cx functional (see the "Model Construction" section).

Rate Effects. To separate rate from size effects, we first consider the former in the large size limit, using a supercell comprising 61440 atoms, equivalent to 16 × 16 × 12 primitive orthorhombic (20-atom) unit cells.

On heating all simulations yield the correct (experimentally observed) sequence of phases irrespective of heating rate. On

https://doi.org/10.1021/acs.jpcc.3c01542
J. Phys. Chem. C 2023, 127, 13773−13781

cooling, this sequence is reversed again regardless of rate. At the cubic-to-tetragonal transition, for a small number of simulations, one can, however, observe the simultaneous formation of multiple tetragonal domains with incompatible orientations, which can lead to the formation of domain boundaries. Since the moving of these boundaries involves a nucleation-and-growth mechanism, they remain in the simulated structure upon cooling.

The temperatures for the transitions between the perovskite phases can be readily obtained from the lattice parameters (Figure 1a,b), revealing a strong dependence on the heating/cooling rate. For rates below approximately 60 K/ns, the hysteresis between heating and cooling runs is 15 K or less and no longer varies systematically with the rate (Figure 1c). By contrast, for the largest rate of 600 K/ns considered here, which is only slightly larger than values used in some earlier MLP studies,[19,26] one observes a hysteresis of about 100 K for both the lower and higher temperature transitions. In addition, the transition itself is smeared out in temperature, which is particularly apparent for the orthorhombic-to-tetragonal transition (Figure 1a).

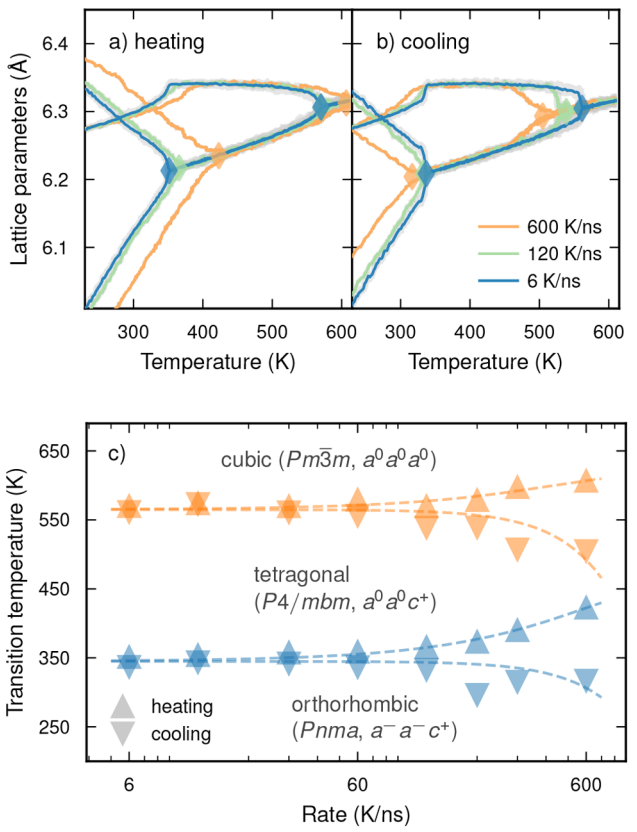

Figure 1. Convergence with heating/cooling rate. Lattice parameters for $CsPbI_3$ as a function of temperature from MD simulations with varying (a) heating and (b) cooling rates for supercells comprising 61440 atoms. The transition temperatures extracted from these data are indicated by diamonds. The gray lines show the raw data, whereas the colored lines show the data after application of a Hamming window of 0.6 K (see Figure S4). (c) Transition temperatures as a function of heating/cooling rate. Dashed lines are guides to the eye. All results were obtained using the full model (see the "Model Construction" section) based on the vdW-DF-cx exchange-correlation functional.

We also observed similar trends for the other materials and models studied in this work. We therefore conclude that rates below 60 K/ns are recommended in order to achieve convergence of the transition temperatures for this class of materials.

Size Effects. Next we examine the impact of the supercell size on the temperature dependence of the lattice parameters and the transition temperatures. First, simulations were carried out at a heating/cooling rate of 6 K/ns using structures comprising 1280 atoms (4 × 4 × 4) primitive orthorhombic unit cells), 7680 atoms (8 × 8 × 6), 23040 atoms (12 × 12 × 8), or 61440 atoms (16 × 16 × 12).

For the smallest supercell (1280 atoms), one notices a marked deviation from the (reference) lattice parameter parameter data from the largest supercell (61440 atoms) around the cubic-tetragonal phase transition (Figure 2a,b).

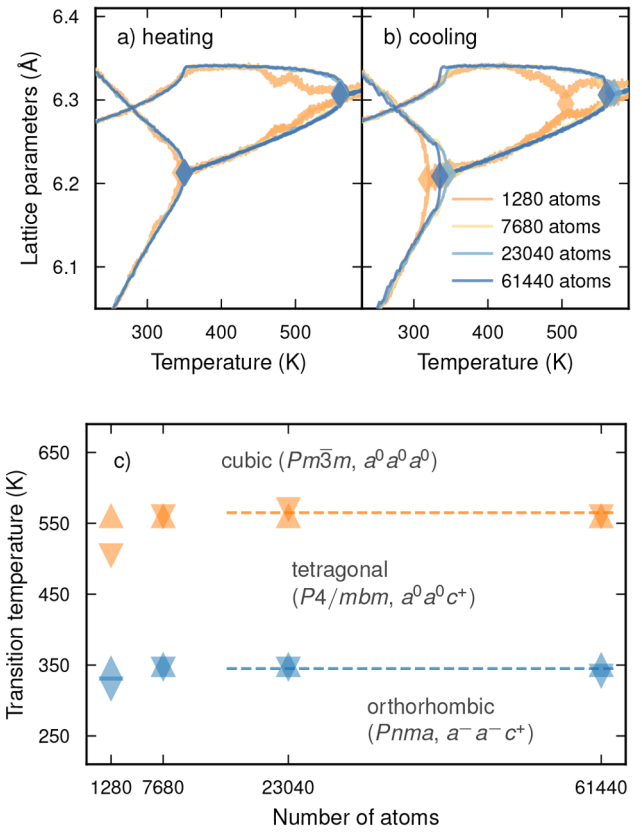

Figure 2. Convergence with supercell size. Lattice parameters for $CsPbI_3$ as a function of temperature from MD simulations during (a) heating and (b) cooling at a rate of R = 6 K/ns for different supercells. The transition temperatures extracted from these data are indicated by diamonds. A Hamming window of 0.6 K was applied. (c) Transition temperatures as a function of supercell size. Dashed lines are guides to the eye. All results were obtained using the full model (see the "Model Construction" section) based on the vdW-DF-cx exchange-correlation functional.

This deviation is, however, absent for the next larger structure, which comprises 7680 atoms, and at this size, the transition temperatures are already converged to within 10 K of the results for the largest supercell (Figure 2c).

A key characteristic of a phase transition that is at least partly continuous is a peak or kink in the heat capacity. The heat capacity can be readily extracted from fluctuations of the

https://doi.org/10.1021/acs.jpcc.3c01542
J. Phys. Chem. C 2023, 127, 13773−13781

energy in MD simulations. For the present purpose, this is, however, impractical as the transition is very sharp in temperature and the temperature range of interest is wide. Here, we therefore compute the heat capacity instead by numerically differentiating the potential energy from heating/cooling runs, i.e., $C_p = dH/dT \approx \Delta H/\Delta T$. This requires averaging of the data in order to obtain numerically well behaved results. To this end, we first apply a Hamming window of 0.6 K to the energy-vs-temperature data. The resulting data is numerically differentiated, after which the data is smoothened again using a Hamming window of 6 K. The Hamming window sizes are chosen to be sufficiently large to remove noise and small enough to avoid removing features (Figure S5).

For the largest system size (61440 atoms), the phase transitions are clearly visible as peaks in the temperature dependence of the heat capacity (Figure 3). These features become, however, less distinct with decreasing system size as fluctuations increase.

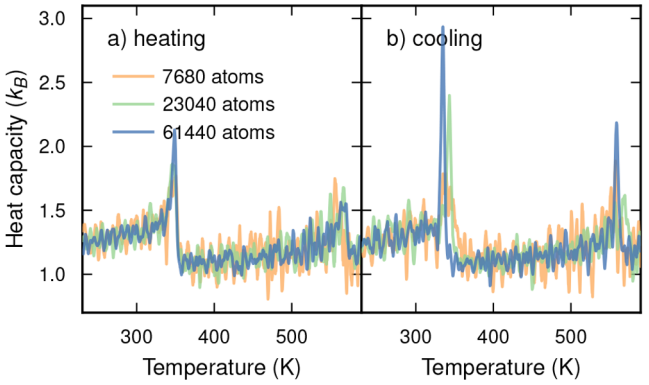

Figure 3. Convergence of heat capacity with supercell size isobaric heat capacity of $CsPbI_3$ as a function of temperature for different supercell sizes obtained through numerical differentiation as detailed in the text. The phase transitions are visible as peaks in the heat capacity. All results were obtained using the full model (see the "Model Construction" section) based on the vdW-DF-cx exchange-correlation functional.

The analysis presented in this section suggests that supercells with at least about 10000 atoms can be expected to yield accurate lattice parameters and transition temperatures within about 10 K of the converged results. Extracting the temperature dependence of the heat capacity still requires larger systems still. Even for the largest systems considered here (61440 atoms), the noise level is rather high, but the data still allow one to accurately extract phase transition temperatures from the heat capacity data.

Model Uncertainty. Having established heating/cooling rates and system sizes that yielded converged results for lattice parameters and transition temperatures, we can now address model uncertainty. To this end, we resort to ensemble models. The latter comprise five separate models constructed using five distinct 90−10 splits of the training data (see the "Model Construction" section). All simulations in this section were carried out using supercells with 61440 atoms and a heating/cooling rate of 6 K/ns. Once again, we use $CsPbI_3$ and models trained using reference data generated by the vdW-DF-cx functional as a representative example.

The uncertainty of the model predictions can be estimated by considering the standard deviation over the model ensemble (Figure 4a,b). At 100 K this approach yields an

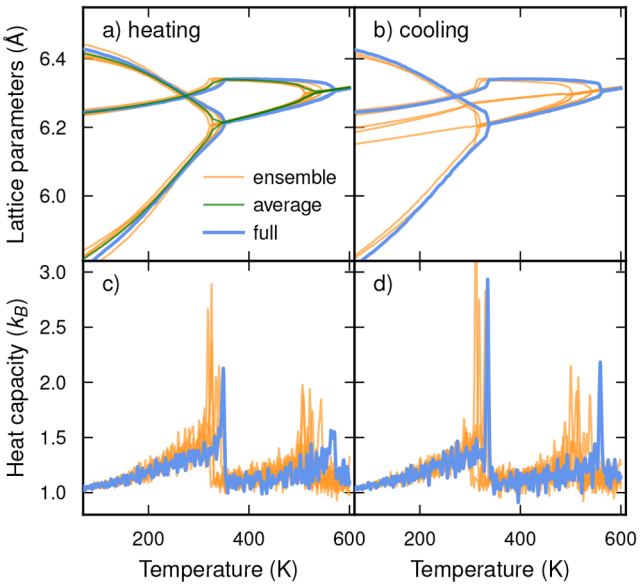

Figure 4. Assessing model uncertainty through ensemble of models. (a,b) Lattice parameters and (c,d) heat capacity as a function of temperature during (a,c) heating and (b,d) cooling from full (blue lines), ensemble models (orange lines), and the average over the later (green lines). All results are for $CsPbI_3$ using models based on the vdW-DF-cx exchange-correlation functional.

uncertainty of up to 0.02 Å depending on direction. This value diminishes, however, quickly with temperature to a level of 0.003 Å in the tetragonal and even less than 0.002 Å in the cubic phases (Figure S6).

Away from the phase transitions, the heat capacity curves from the different models agree well with each other (Figure 4). The actual transition temperatures, corresponding to the position of the peaks in the heat capacity curves, obtained from the full model (and the model ensemble) are 348 K (329(11) K) and 549 K (521(15) K) on heating and 334 K (317(19) K) and 549 K (511(20) K) on cooling. The agreement between the results obtained using the full model and the model ensemble support the good convergence of the models with respect to training data. The remaining hysteresis can be attributed to the mixed first-/continuous-order character, which is evident from the very small but nonzero latent heat associated with these transitions.[52−55]

We can thus estimate the error in the transition temperatures due to model uncertainty to be on the order of 30 K. In combination with the model performance measures (see the "Model Construction" section) and the very good agreement with the DFT reference data, this provides strong evidence that the NEP models constructed are accurate representations of the DFT potential energy landscape in the regions of configuration space included here. They can thus be used to analyze the performance of different XC functionals with respect to the finite temperature behavior of $CsPbI_3$ and the other materials considered here (see the "Impact of XC Functional and Extension to other Halides" section).

Impact of XC Functional and Extension to Other Halides. We can now apply the framework established above to predict transition temperatures for $CsPbI_3$ using different

https://doi.org/10.1021/acs.jpcc.3c01542
J. Phys. Chem. C 2023, 127, 13773−13781

XC functionals for generating reference data and compare the results to experimental data. To this end, we use the same computational settings in terms of system size and heating/cooling rate as in the analysis of the model uncertainty.

The results show that the vdW-DF-cx, SCAN+rVV10, and LDA functionals yield temperatures for the tetragonal-to-cubic transition in good agreement with experimental data (Figure 5).[9] They, however, notably underestimate the orthogonal-to-

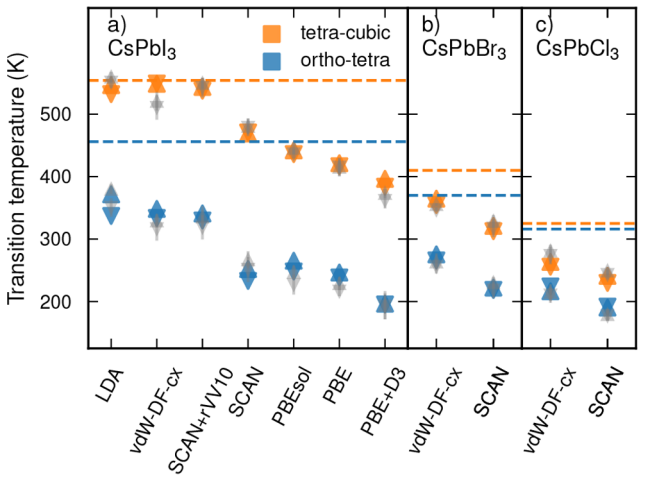

Figure 5. Transition temperatures from MD simulations in comparison with experiment. Data were obtained using heating (upward triangles) and cooling runs (downward triangles) with rates of 6 K/ns for supercells comprising 61440 atoms. Colored and gray symbols indicate results obtained using full models and model ensembles, respectively. In the latter case, the uncertainty calculated as the standard deviation over the ensemble is indicated by vertical bars. Experimental transition temperatures taken from refs 9, 56, and 57 are shown by horizontal dashed lines.

tetragonal transition temperature. It should be noted that the apparently good agreement obtained using the LDA is likely the result of a fortuitous cancellation of errors, a behavior that has also been observed for, e.g., van-der-Waals bonded materials.

The remaining functionals (SCAN, PBEsol, PBE, and PBE+D3) markedly underestimate both transition temperatures by as much as 200 K. We note that the agreement improves from PBE via PBEsol and SCAN to vdW-DF-cx, which mirrors the trends observed previously for transition metals.[58] Conversely for the lattice parameters, with the exception of the LDA functional, one observes a systematic overestimation relative to the experiment (Figure 6) with a similar trend. The closest agreement is obtained using the vdW-DF-cx functional, for which the lattice parameters of the cubic phase are overestimated by only 0.02−0.04 Å in the high-temperature limit.

Finally, we extend our investigation to $CsPbBr_3$ and $CsPbCl_3$ including SCAN and vdW-DF-cx functionals. As for $CsPbI_3$ the transition temperatures (Figure 5b,c) and lattice parameters (Figure 6b,c) are systematically underestimated and overestimated, respectively. The thermal expansion is, however, captured well by all functionals.

We conclude by noting that all of the XC functionals considered here yield the correct sequence of phases, yet there is a tendency to underestimate the transition temperatures (Figure 5) and overestimate the lattice parameters (Figure 6).

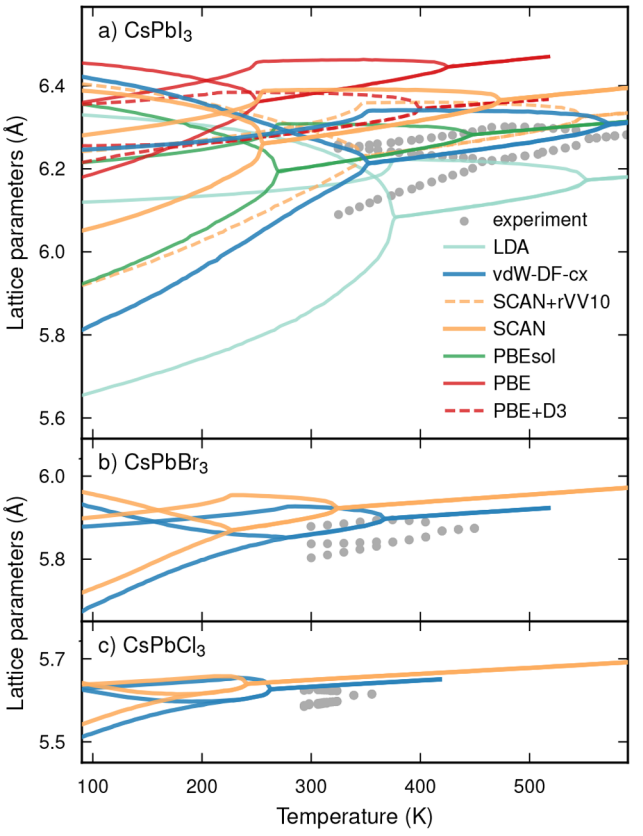

Figure 6. Lattice parameters as a function of temperature from simulation in comparison with experiment. Data were obtained using full NEP models trained using different XC functionals in comparison. Experimental data from refs 9, 56, and 57

Transition to δ-Phase. It is experimentally well established that the perovskite phases of $CsPbI_3$ are only metastable at low temperatures as the actual ground state structure of the material is the so-called δ-phase.[59] We therefore also computed the transition temperature between the cubic perovskite and the δ-phase by free energy integration (see Figure S7 for the free energy curves).

The transition temperature obtained for $CsPbI_3$ by the vdW-DF-cx model of 633 K with an estimated uncertainty of 20 to 40 K is in good agreement with experimental values of around 600 K (Table 2). The SCAN+rVV10 and LDA models yield transition temperatures of 582 and 573 K, respectively, also in good agreement with experiment. The SCAN, PBE, PBE+D3, and PBEsol models yield lower values that are considerably

Table 2. Temperatures for the Transition between the δ-Phase and the Cubic Perovskite Phase[a]

	$CsPbI_3$	$CsPbBr_3$
experiment	∼600	
vdW-DF-cx	633	313
SCAN	433	158
SCAN+rVV10	582	
LDA	573	
PBE	308	
PBEsol	373	
PBE+D3	405	

[a]Experimental data from refs 60−62.

https://doi.org/10.1021/acs.jpcc.3c01542
J. Phys. Chem. C 2023, 127, 13773−13781

smaller than the experimental data. These estimated transition temperatures correlate quite well with the energy differences between the δ-phase and perovskite phases (Table S4).

In the case of $CsPbBr_3$, the δ-phase is the most stable structure at 0 K, according to both the DFT and NEP calculations. The energy difference (Table S3) is, however, much smaller than that for $CsPbI_3$ (Table S4), leading to lower transition temperatures that are predicted to be 310 and 151 K according to the vdW-DF-cx and SCAN models, respectively. We are unaware of experimental measurements of the transition temperature in $CsPbBr_3$, which given the present predictions might actually be close to or below room temperature and thus are difficult to observe.

For $CsPbCl_3$ the DFT calculations yield energy differences between perovskite and δ-phases close to zero (Table S2), suggesting that the δ-phase is actually not the most stable phase under any conditions or only at extremely low temperatures.

DISCUSSION

We have systematically analyzed four key sources of error in atomic scale simulations of phase transitions of inorganic halide perovskites, related respectively to (1) sampling time, (2) system size, (3) model uncertainty, and (4) the underlying XC functional. Based on these results, it is recommended to use heating/cooling rates of at most approximately 60 K/ns but preferably even lower and system sizes comprising at least a couple ten thousands of atoms, corresponding to a few thousand primitive unit cells. We expect that these guidelines are not limited to inorganic halide perovskites but should also be heeded when modeling the dynamics of other perovskites and related systems.

The model uncertainty was assessed using ensembles of models from which uncertainty estimates for, e.g., transition temperatures and lattice parameters, can be estimated. The results show that by careful model construction, the model uncertainty can be reduced to a level that allows one to quantitatively discriminate the performance of different XC functionals.

Using this approach, we found that while the vdW-DF-cx, SCAN+rVV10, and LDA functionals yield temperatures for the tetragonal-to-cubic transition in good agreement with experimental data, the other XC functionals (namely, SCAN, PBEsol, PBE, and PBE+D3) underestimate it significantly. At the same time, all functionals considered here underestimate the orthogonal-to-tetragonal transition. Moreover all functionals except for LDA overestimate the lattice parameters at finite temperature, with vdW-DF-cx and SCAN+rVV10 achieving rather close agreement with experiment.

The opposite trends observed when going from SCAN to SCAN+rVV10 and from PBE to PBE+D3 suggest that the inclusion of van-der-Waals interactions does not *per se* improve a functional, but rather one should consider the resulting combined functional on its own.

Considering both transition temperatures and lattice parameters, the best overall agreement is obtained for the vdW-DF-cx and SCAN+rVV10 functionals, which, in particular, outperform the SCAN functional. In pioneering work on the use of MLPs for probing the dynamics of halide perovskite, the latter functional had been suggested as achieving a good match with experiment.[19,26,63,64] Our analysis suggests that the good agreement was likely fortuitous and probably the result of using high rates and small system sizes (see Figure S8 for a more detailed comparison).

This raises the question how, for example, hybrid functionals or the random phase approximation would perform with regard to the finite temperature properties and dynamics of these materials.[13,27,65] In the present work, we included a relatively large set of structures and supercells that would pose a considerable computational challenge for either one of these methods. As noted above (see the "Model Construction" section), one can, however, expect that the number of training structures can be considerably reduced without a notable loss in model accuracy by using active learning. This strategy could be combined with principal component analysis to identify regions with very dense sampling[37] or entropy maximization[66] to reduce the training set size even further, eventually allowing one to build NEP or other MLP models that can represent such more accurate electronic structure methods.

Finally, we note that the accuracy of the models presented here in combination with the very high computational efficiency provided by the implementation on GPUs, now enables one to sample the dynamics of these and related materials with unprecedented time resolution and accuracy.

ASSOCIATED CONTENT

Data Availability Statement

The DFT data and NEP models generated in this study are openly available via Zenodo at 10.5281/zenodo.7454223.

Supporting Information

The Supporting Information is available free of charge at https://pubs.acs.org/doi/10.1021/acs.jpcc.3c01542.

Training and validation of the MLPs; additional figures on how cooling/heating rates and system size influence thermodynamic properties; calculated free energies of cubic perovskite and the δ-phase; energy differences between all relevant phases with the MLPs and DFT (PDF)

AUTHOR INFORMATION

Corresponding Authors

Erik Fransson − *Department of Physics, Chalmers University of Technology, SE-41296 Gothenburg, Sweden;* orcid.org/0000-0001-5262-3339; Email: erikfr@chalmers.se

Paul Erhart − *Department of Physics, Chalmers University of Technology, SE-41296 Gothenburg, Sweden;* orcid.org/0000-0002-2516-6061; Email: erhart@chalmers.se

Author

Julia Wiktor − *Department of Physics, Chalmers University of Technology, SE-41296 Gothenburg, Sweden;* orcid.org/0000-0003-3395-1104

Complete contact information is available at: https://pubs.acs.org/10.1021/acs.jpcc.3c01542

Author Contributions

All authors contributed equally.

Notes

The authors declare no competing financial interest.

ACKNOWLEDGMENTS

This work was funded by the Swedish Research Council (grant numbers 2018-06482, 2019-03993, 2020-04935, 2021-05072) and the Chalmers Initiative for Advancement of Neutron and

Synchrotron Techniques. The computations were enabled by resources provided by the National Academic Infrastructure for Supercomputing in Sweden (NAISS) and the Swedish National Infrastructure for Computing (SNIC) at NSC, C3SE, and PDC partially funded by the Swedish Research Council through grant agreement nos. 2022-06725 and 2018-05973.

REFERENCES

(1) Kojima, A.; Teshima, K.; Shirai, Y.; Miyasaka, T. Organometal halide perovskites as visible-light sensitizers for photovoltaic cells. *J. Am. Chem. Soc.* **2009**, *131*, 6050.
(2) Kim, H.-S.; Lee, C.-R.; Im, J.-H.; Lee, K.-B.; Moehl, T.; Marchioro, A.; Moon, S.-J.; Humphry-Baker, R.; Yum, J.-H.; Moser, J. E.; et al. Lead iodide perovskite sensitized all-solid-state submicron thin film mesoscopic solar cell with efficiency exceeding 9%. *Sci. Rep.* **2012**, *2*, 591.
(3) Hodes, G. Perovskite-based solar cells. *Science* **2013**, *342*, 317.
(4) Van Le, Q.; Jang, H. W.; Kim, S. Y. Recent advances toward high-efficiency halide perovskite light-emitting diodes: Review and perspective. *Small Methods* **2018**, *2*, 1700419.
(5) Tyson, T.; Gao, W.; Chen, Y.-S.; Ghose, S.; Yan, Y. Large thermal motion in halide perovskites. *Sci. Rep.* **2017**, *7* (1), 9401.
(6) Liu, J.; Du, J.; Phillips, A. E.; Wyatt, P. B.; Keen, D. A.; Dove, M. T. Neutron powder diffraction study of the phase transitions in deuterated methylammonium lead iodide. *J. Phys.: Condens. Matter* **2022**, *34*, 145401.
(7) Yaffe, O.; Guo, Y.; Tan, L. Z.; Egger, D. A.; Hull, T.; Stoumpos, C. C.; Zheng, F.; Heinz, T. F.; Kronik, L.; Kanatzidis, M. G.; et al. Local polar fluctuations in lead halide perovskite crystals. *Phys. Rev. Lett.* **2017**, *118*, 136001.
(8) Marronnier, A.; Lee, H.; Geffroy, B.; Even, J.; Bonnassieux, Y.; Roma, G. Structural instabilities related to highly anharmonic phonons in halide perovskites. *J. Phys. Chem. Lett.* **2017**, *8*, 2659.
(9) Marronnier, A.; Roma, G.; Boyer-Richard, S.; Pedesseau, L.; Jancu, J.-M.; Bonnassieux, Y.; Katan, C.; Stoumpos, C. C.; Kanatzidis, M. G.; Even, J. Anharmonicity and disorder in the black phases of cesium lead iodide used for stable inorganic perovskite solar cells. *ACS Nano* **2018**, *12*, 3477.
(10) Bechtel, J. S.; Thomas, J. C.; Van der Ven, A. Finite-temperature simulation of anharmonicity and octahedral tilting transitions in halide perovskites. *Physical Review Materials* **2019**, *3*, 113605.
(11) Carignano, M. A.; Kachmar, A.; Hutter, J. Thermal effects on CH3NH3PbI3 perovskite from ab initio molecular dynamics simulations. *J. Phys. Chem. C* **2015**, *119*, 8991.
(12) Wiktor, J.; Rothlisberger, U.; Pasquarello, A. Predictive determination of band gaps of inorganic halide perovskites. *J. Phys. Chem. Lett.* **2017**, *8*, 5507.
(13) Bokdam, M.; Lahnsteiner, J.; Ramberger, B.; Schäfer, T.; Kresse, G. Assessing Density Functionals Using Many Body Theory for Hybrid Perovskites. *Phys. Rev. Lett.* **2017**, *119*, 145501.
(14) Mladenović, M.; Vukmirović, N. Effects of thermal disorder on the electronic structure of halide perovskites: insights from md simulations. *Phys. Chem. Chem. Phys.* **2018**, *20*, 25693.
(15) Zhu, X.; Caicedo-Dávila, S.; Gehrmann, C.; Egger, D. A. Probing the disorder inside the cubic unit cell of halide perovskites from first-principles. *ACS Appl. Mater. Interfaces* **2022**, *14*, 22973.
(16) Gebhardt, J.; Elsässer, C. The electronic structure of Cs2AgBiBr6 at room temperature. *Physica Status Solidi (b)* **2022**, *259*, 2200124.
(17) Girdzis, S. P.; Lin, Y.; Leppert, L.; Slavney, A. H.; Park, S.; Chapman, K. W.; Karunadasa, H. I.; Mao, W. L. Revealing local disorder in a silver-bismuth halide perovskite upon compression. *J. Phys. Chem. Lett.* **2021**, *12*, 532.
(18) Cannelli, O.; Wiktor, J.; Colonna, N.; Leroy, L.; Puppin, M.; Bacellar, C.; Sadykov, I.; Krieg, F.; Smolentsev, G.; Kovalenko, M. V.; et al. Atomic-level description of thermal fluctuations in inorganic lead halide perovskites. *J. Phys. Chem. Lett.* **2022**, *13*, 3382.
(19) Jinnouchi, R.; Lahnsteiner, J.; Karsai, F.; Kresse, G.; Bokdam, M. Phase transitions of hybrid perovskites simulated by machine-learning force fields trained on the fly with Bayesian inference. *Phys. Rev. Lett.* **2019**, *122*, 225701.
(20) Lahnsteiner, J.; Jinnouchi, R.; Bokdam, M. Long-range order imposed by short-range interactions in methylammonium lead iodide: Comparing point-dipole models to machine-learning force fields. *Phys. Rev. B* **2019**, *100*, No. 094106.
(21) Thomas, J. C.; Bechtel, J. S.; Natarajan, A. R.; Van der Ven, A. Machine learning the density functional theory potential energy surface for the inorganic halide perovskite CsPbBr3. *Phys. Rev. B* **2019**, *100*, 134101.
(22) Zhou, G.; Chu, W.; Prezhdo, O. V. Structural deformation controls charge losses in MAPbI3: Unsupervised machine learning of nonadiabatic molecular dynamics. *ACS Energy Letters* **2020**, *5*, 1930.
(23) Mangan, S. M.; Zhou, G.; Chu, W.; Prezhdo, O. V. Dependence between structural and electronic properties of CsPbI3: Unsupervised machine learning of nonadiabatic molecular dynamics. *J. Phys. Chem. Lett.* **2021**, *12*, 8672.
(24) Bokdam, M.; Lahnsteiner, J.; Sarma, D. D. Exploring librational pathways with on-the-fly machine-learning force fields: Methylammonium molecules in MAPbX3 (X= I, Br, Cl) perovskites. *J. Phys. Chem. C* **2021**, *125*, 21077.
(25) Grüninger, H.; Bokdam, M.; Leupold, N.; Tinnemans, P.; Moos, R.; De Wijs, G. A.; Panzer, F.; Kentgens, A. P. M. Microscopic (dis)order and dynamics of cations in mixed FA/MA lead halide perovskites. *J. Phys. Chem. C* **2021**, *125*, 1742.
(26) Lahnsteiner, J.; Bokdam, M. Anharmonic lattice dynamics in large thermodynamic ensembles with machine-learning force fields: CsPbBr3 a phonon liquid with Cs rattlers. *Phys. Rev. B* **2022**, *105*, No. 024302.
(27) Braeckevelt, T.; Goeminne, R.; Vandenhaute, S.; Borgmans, S.; Verstraelen, T.; Steele, J. A.; Roeffaers, M. B. J.; Hofkens, J.; Rogge, S. M. J.; Van Speybroeck, V. Accurately Determining the Phase Transition Temperature of CsPbI3 via Random-Phase Approximation Calculations and Phase-Transferable Machine Learning Potentials. *Chem. Mater.* **2022**, *34*, 8561.
(28) Fransson, E.; Rosander, P.; Eriksson, F.; Rahm, J. M.; Tadano, T.; Erhart, P. Probing the limits of the phonon quasi-particle picture: The transition from underdamped to overdamped dynamics in $CsPbBr_3$. *arXiv (Quantum Physics)*,12 Oct 2001, arXiv:2211.08197. DOI: 10.1080/09500340110105975.
(29) Ghosh, D.; Walsh Atkins, P.; Islam, M. S.; Walker, A. B.; Eames, C. Good vibrations: Locking of octahedral tilting in mixed-cation iodide perovskites for solar cells. *ACS Energy Letters* **2017**, *2*, 2424.
(30) Dion, M.; Rydberg, H.; Schröder, E.; Langreth, D. C.; Lundqvist, B. I. Van der waals density functional for general geometries. *Phys. Rev. Lett.* **2004**, *92*, 246401.
(31) Berland, K.; Hyldgaard, P. Exchange functional that tests the robustness of the plasmon description of the van der waals density functional. *Phys. Rev. B* **2014**, *89*, No. 035412.
(32) Sun, J.; Ruzsinszky, A.; Perdew, J. P. Strongly Constrained and Appropriately Normed Semilocal Density Functional. *Phys. Rev. Lett.* **2015**, *115*, No. 036402.
(33) Peng, H.; Yang, Z.-H.; Perdew, J. P.; Sun, J. Versatile van der waals density functional based on a meta-generalized gradient approximation. *Physical Review X* **2016**, *6*, No. 041005.
(34) Perdew, J. P.; Ruzsinszky, A.; Csonka, G. I.; Vydrov, O. A.; Scuseria, G. E.; Constantin, L. A.; Zhou, X.; Burke, K. Restoring the density-gradient expansion for exchange in solids and surfaces. *Phys. Rev. Lett.* **2008**, *100*, 136406.
(35) Perdew, J. P.; Burke, K.; Ernzerhof, M. Generalized gradient approximation made simple. *Phys. Rev. Lett.* **1996**, *77*, 3865.
(36) Grimme, S.; Antony, J.; Ehrlich, S.; Krieg, H. A consistent and accurate ab initio parametrization of density functional dispersion correction (DFT-D) for the 94 elements H-Pu. *J. Chem. Phys.* **2010**, *132*, 154104.

(37) Fan, Z.; Wang, Y.; Ying, P.; Song, K.; Wang, J.; Wang, Y.; Zeng, Z.; Xu, K.; Lindgren, E.; Rahm, J. M.; Gabourie, A. J.; Liu, J.; Dong, H.; Wu, J.; Chen, Y.; Zhong, Z.; Sun, J.; Erhart, P.; Su, Y.; Ala-Nissila, T. GPUMD: A package for constructing accurate machine-learned potentials and performing highly efficient atomistic simulations. *J. Chem. Phys.* **2022**, *157*, 114801.
(38) Fan, Z.; Zeng, Z.; Zhang, C.; Wang, Y.; Song, K.; Dong, H.; Chen, Y.; Ala-Nissila, T. Neuroevolution machine learning potentials: Combining high accuracy and low cost in atomistic simulations and application to heat transport. *Phys. Rev. B* **2021**, *104*, 104309.
(39) Drautz, R. Atomic cluster expansion for accurate and transferable interatomic potentials. *Phys. Rev. B* **2019**, *99*, No. 014104.
(40) Wierstra, D.; Schaul, T.; Glasmachers, T.; Sun, Y.; Peters, J.; Schmidhuber, J. Natural evolution strategies. *J. Mach. Learn. Res.* **2014**, *15*, 949.
(41) Eriksson, F.; Fransson, E.; Erhart, P. The Hiphive Package for the Extraction of High-Order Force Constants by Machine Learning. *Advanced Theory and Simulations* **2019**, *2*, 1800184.
(42) *Calorine*, 2022. https://calorine.materialsmodeling.org/ (accessed: 2022−12−18).
(43) Bussi, G.; Donadio, D.; Parrinello, M. Canonical sampling through velocity rescaling. *J. Chem. Phys.* **2007**, *126*, No. 014101.
(44) Bernetti, M.; Bussi, G. Canonical sampling through velocity rescaling. *J. Chem. Phys.* **2020**, *153*, 114107.
(45) Frenkel, D.; Ladd, A. J. C. New Monte Carlo method to compute the free energy of arbitrary solids. Application to the fcc and hcp phases of hard spheres. *J. Chem. Phys.* **1984**, *81*, 3188.
(46) Frenkel, D.; Smit, B. *Understanding Molecular Simulation: From Algorithms to Applications*; Academic Press: San Diego, CA, 2001.
(47) Freitas, R.; Asta, M.; de Koning, M. Nonequilibrium free-energy calculation of solids using LAMMPS. *Comput. Mater. Sci.* **2016**, *112*, 333.
(48) Hjorth Larsen, A.; Jørgen Mortensen, J.; Blomqvist, J.; Castelli, I. E; Christensen, R.; Dułak, M.; Friis, J.; Groves, M. N; Hammer, B.ør.; Hargus, C.; et al. The atomic simulation environment—a python library for working with atoms. *J. Phys.: Condens. Matter* **2017**, *29*, 273002.
(49) Blöchl, P. E. Projector augmented-wave method. *Phys. Rev. B* **1994**, *50*, 17953.
(50) Kresse, G.; Hafner, J. Ab initio molecular dynamics for liquid metals. *Phys. Rev. B* **1993**, *47*, 558.
(51) Kresse, G.; Furthmüller, J. Efficiency of ab-initio total energy calculations for metals and semiconductors using a plane-wave basis set. *Comput. Mater. Sci.* **1996**, *6*, 15.
(52) Hirotsu, S.; Harada, J.; Iizumi, M.; Gesi, K. Structural phase transitions in cspbbr3. *J. Phys. Soc. Jpn.* **1974**, *37*, 1393.
(53) Rodová, M.; Brožek, J.; Knížek, K.; Nitsch, K. *J. Therm. Anal. Calorim.* **2003**, *71*, 667.
(54) Malyshkin, D.; Sereda, V.; Ivanov, I.; Mazurin, M.; Sednev-Lugovets, A.; Tsvetkov, D.; Zuev, A. New phase transition in CsPbBr3. *Mater. Lett.* **2020**, *278*, 128458.
(55) Klarbring, J. Low-energy paths for octahedral tilting in inorganic halide perovskites. *Phys. Rev. B* **2019**, *99*, 104105.
(56) Stoumpos, C. C.; Malliakas, C. D.; Peters, J. A.; Liu, Z.; Sebastian, M.; Im, J.; Chasapis, T. C.; Wibowo, A. C.; Chung, D. Y.; Freeman, A. J.; Wessels, B. W.; Kanatzidis, M. G. Crystal growth of the perovskite semiconductor CsPbBr3: A new material for high-energy radiation detection. *Cryst. Growth Des.* **2013**, *13*, 2722.
(57) He, Y.; Stoumpos, C. C.; Hadar, I.; Luo, Z.; McCall, K. M.; Liu, Z.; Chung, D. Y.; Wessels, B. W.; Kanatzidis, M. G. Demonstration of Energy-Resolved γ-Ray Detection at Room Temperature by the CsPbCl3 Perovskite Semiconductor. *J. Am. Chem. Soc.* **2021**, *143*, 2068.
(58) Gharaee, L.; Erhart, P.; Hyldgaard, P. Finite-temperature properties of nonmagnetic transition metals: Comparison of the performance of constraint-based semilocal and nonlocal functionals. *Phys. Rev. B* **2017**, *95*, No. 085147.
(59) Sutton, R. J.; Filip, M. R.; Haghighirad, A. A.; Sakai, N.; Wenger, B.; Giustino, F.; Snaith, H. J. Cubic or orthorhombic? revealing the crystal structure of metastable black-phase CsPbI3 by theory and experiment. *ACS Energy Letters* **2018**, *3*, 1787.
(60) Dastidar, S.; Hawley, C. J.; Dillon, A. D.; Gutierrez-Perez, A. D.; Spanier, J. E.; Fafarman, A. T. Quantitative Phase-Change Thermodynamics and Metastability of Perovskite-Phase Cesium Lead Iodide. *J. Phys. Chem. Lett.* **2017**, *8*, 1278.
(61) Marronnier, A.; Roma, G.; Boyer-Richard, S.; Pedesseau, L.; Jancu, J.-M.; Bonnassieux, Y.; Katan, C.; Stoumpos, C. C.; Kanatzidis, M. G.; Even, J. Anharmonicity and Disorder in the Black Phases of Cesium Lead Iodide Used for Stable Inorganic Perovskite Solar Cells. *ACS Nano* **2018**, *12*, 3477.
(62) Ke, F.; Wang, C.; Jia, C.; Wolf, N. R.; Yan, J.; Niu, S.; Devereaux, T. P.; Karunadasa, H. I.; Mao, W. L.; Lin, Y. Preserving a robust CsPbI3 perovskite phase via pressure-directed octahedral tilt. *Nat. Commun.* **2021**, *12*, 461.
(63) Paul, A.; Sun, J.; Perdew, J. P.; Waghmare, U. V. Accuracy of first-principles interatomic interactions and predictions of ferroelectric phase transitions in perovskite oxides: Energy functional and effective Hamiltonian. *Phys. Rev. B* **2017**, *95*, No. 054111.
(64) Zhang, Y.; Sun, J.; Perdew, J. P.; Wu, X. Comparative first-principles studies of prototypical ferroelectric materials by LDA. *GGA, and SCAN meta-GGA, Physical Review B* **2017**, *96*, No. 035143.
(65) Verdi, C.; Ranalli, L.; Franchini, C.; Kresse, G. Quantum paraelectricity and structural phase transitions in strontium titanate beyond density-functional theory. *Phys. Rev. Materials* **2023**, *7*, L030801.
(66) Karabin, M.; Perez, D. An entropy-maximization approach to automated training set generation for interatomic potentials. *J. Chem. Phys.* **2020**, *153*, No. 094110.

https://doi.org/10.1021/acs.jpcc.3c01542
J. Phys. Chem. C 2023, 127, 13773−13781